All-Optical Generation and Time-Resolved Polarimetry of Magnetoacoustic Resonances via Transient Grating Spectroscopy

P. Carrara,[1,2] M. Brioschi,[1,2] E. Longo,[3] D. Dagur,[1,4] V. Polewczyk,[1] G. Vinai,[1] R. Mantovan,[3] M. Fanciulli,[5] G. Rossi,[2] G. Panaccione,[1,*] and R. Cucini[1]

[1] *Istituto Officina dei Materiali (IOM), Consiglio Nazionale delle Ricerche (CNR), Area Science Park, Trieste I-34149, Italy*

[2] *Dipartimento di Fisica, Università degli Studi di Milano, Via Celoria 16, Milano 20133, Italy*

[3] *Institute for Microelectronics and Microsystems, CNR-IMM Unit of Agrate Brianza, Via C. Olivetti 2, Agrate Brianza 20864, Italy*

[4] *Dipartimento di Fisica, Università degli Studi di Trieste, Via Valerio 2, Trieste 34127, Italy*

[5] *Dipartimento di Scienza dei Materiali, Università degli Studi di Milano Bicocca, Milano IT-20125, Italy*

(Received 5 May 2022; revised 28 June 2022; accepted 28 July 2022; published 5 October 2022)

The generation and control of surface acoustic waves (SAWs) in a magnetic material are objects of an intense research effort focused on magnetoelastic properties, with fruitful ramifications in spin-wave-based quantum logic and magnonics. We implement a transient grating setup to optically generate SAWs also seeding coherent spin waves via magnetoelastic coupling in ferromagnetic media. In this work we report on SAW-driven ferromagnetic resonance (FMR) experiments performed on polycrystalline Ni thin films in combination with time-resolved Faraday polarimetry, which allows extraction of the value of the effective magnetization and of the Gilbert damping. The results are in full agreement with measurements on the very same samples from standard FMR. Higher-order effects due to parametric modulation of the magnetization dynamics, such as down-conversion, up-conversion, and frequency mixing, are observed, testifying the high sensitivity of this technique.

DOI: 10.1103/PhysRevApplied.18.044009

I. INTRODUCTION

The use of the spin degree of freedom for memory storage and logic computation is the goal of spintronic and magnonic research. Nowadays, much effort is devoted to the exploitation of spin waves (SWs), where the absence of carriers and scattering ensures no Joule dissipation and a wide range of working frequencies, in close similarity to photonics [1–3]. Controlling amplitude and phase of spin excitations is hampered by decoherence phenomena and magnetic damping upon propagation, and efficient methods for producing SWs in magnetic materials are needed.

Magnetoelastic coupling proved to be a promising pathway for the control of magnetic properties of materials and devices [4], and surface acoustic waves (SAWs) have been extensively used to investigate magnetoacoustic and phonon-magnon coupling in ferromagnetic thin films, due to the (quasi)degeneracy of SAW and SW dispersion in the few GHz and μm^{-1} ranges [5–9]. In fact, SAWs can induce coherent and long-living SWs through inverse magnetostriction, which translates in a variation of the magnetization due to lattice deformations. Recently, interdigitated transducers on piezoelectric substrates [6,10] have been employed to elastically pump SWs. These devices have proven to be very effective in achieving all-elastically driven ferromagnetic resonance (FMR), where rf SAW-induced elastic deformation replaces the traditionally applied rf electromagnetic field. However, these approaches have some limitations, e.g., a restricted flexibility in the explorable frequency range, due to the defined pattern of the transducers, and their in-contact operation.

Starting from 2015, Tobey and co-workers reported an all-optical approach for both the excitation of SAWs and the time-resolved (TR) detection of the magnetization of ferromagnetic thin films, thus demonstrating a contactless and noninvasive tool for studying magnetoacoustic effects and SW propagation [11]. They exploited the transient grating (TG) spectroscopy, a nonlinear optical pump-probe technique belonging to the class of four-wave mixing spectroscopy [12–20], scarcely applied to magnetic

*panaccione@iom.cnr.it

study [7,21–24]. TG proves to be efficient in generating coherent SWs in a ferromagnetic medium, and allows full tunability of SAW frequency by varying the grating pitch, placing this technique in the useful frequency window (few GHz) of SAW-driven magnonics. Furthermore, it is possible to simultaneously probe acoustic and magnetic dynamics with sub-ps time resolution in the same TG setup.

Expanding on that approach, we implement a versatile setup to perform a systematic study of TG-SAW-driven FMR on polycrystalline Ni thin films of various thickness, that are grown on different substrates, by combining TG excitation and TR Faraday polarimetry. In this way, we are sensitive to the out-of-plane (OOP) component of the Ni magnetization vector, obtaining information on the coupling between the acoustic and the magnetic degrees of freedom. Our results confirm the observations of Tobey's group on similar samples [7,25]; we also quantitatively estimate the effective magnetization M_{eff} and the Gilbert damping α for the investigated samples. In the case of Ni on CaF_2 substrate (indicated as Ni/CaF_2), we further compare our SAW-driven FMR results with standard FMR ones on the very same samples, obtaining fully consistent results. Finally, the high sensitivity of the TG technique is confirmed by (i) SAW-FMR results obtained on Ni/SiO_2, where the combination of thermoelastic efficiency and magneto-optical sensitivity gives an overall figure of merit ($\mathcal{F}$) 4 times smaller than in Ni/CaF_2 (see Table I below and discussion thereof) and (ii) fast Fourier transform (FFT) analysis of the TR-Faraday signals revealing higher-order parametric resonances (frequency mixing), also in agreement with what has been observed in Ref. [25,26].

II. EXPERIMENTAL SETUP

The experimental setup is presented in Fig. 1; it is conceived to easily switch from TG spectroscopy in transmission geometry to Faraday polarimetry.

The laser source is a Yb:KGW fiber-based laser (Pharos, Light Conversion), available at NFFA-SPRINT laboratory in Trieste, Italy [27]. The laser source delivers pulses at 1028 nm, 300 fs and approximately 5 nm in bandwidth; the adjustable repetition rate is set to 50 kHz. The pump beams are obtained from the fundamental of the laser; the probe beam (514 nm, 250 fs) is obtained by second-harmonic generation of the fundamental in a 2-mm-thick BBO crystal. Energy is set to 30 nJ for each pump and 200 pJ for the probe. The spot size is about 40 μm in diameter for the pump and somewhat smaller for the probe, giving a fluence on the sample 5 mJ/cm^2 for the pump and 0.18 mJ/cm^2 for the probe. The delay between the pump and probe is controlled by routing the probe towards a corner cube retroflector mounted on a 500-mm delay line (maximum time delay approximately equal to 3.3 ns). The pump and the probe beams, red and green, respectively, in Fig. 1, lie in a plane normal to the sample surface and are *s* polarized. They are overlapped on a dichroic mirror (DM in the sketch) and focused onto a phase mask [28]. The diffracted orders are focused on the sample by a pair of achromatic doublets (D1, D2) in confocal configuration. The first diffraction orders of the pump [$m = \pm 1$ in Fig. 1(a)] interfere on the sample, generating the TG. Briefly, the excitation mechanism involves absorption of the pump photons and subsequent thermal expansion, which generates a pattern of standing SAWs, given the stripy interference pattern.

TABLE I. Thermoelastic efficiency and figure of merit (both normalized to the CaF_2 value) and relevant parameters [see Eqs. (2) and (3)] for different substrates (mainly transparent). The substrates of our choice are highlighted in bold.

Substrate	α_{th} (10^{-6} K^{-1})	ν	c_{th} (J/kg K)	k_{th} (W/m K)	η_{norm}	$\mathcal{F}_{\text{norm}}$
CaF_2[a]	18.85	0.26	854	9.7	1	1
Al_2O_3[b]	5.8	0.21–0.33	753	41.9	0.31–0.41	0.07–0.09
$SrTiO_3$	9.4[c]	0.24[d]	518[d]	12[c]	0.79	0.64
MgO[e]	9–12	0.35–0.37	880–1030	30–60	0.48–0.79	0.08–0.26
SiO_2 (Fused silica)[f]	0.54–0.57	0.15–0.16	700–750	1.0–1.5	0.03	0.17–0.29
Soda Lime[g]	9.5	0.24	500	0.7–1.3	0.82	6.15–11.4
Si[h]	7-8	0.27	668-715	84–100	0.45–0.55	0.04–0.06

[a][37]
[b][38]
[c][39]
[d][40]
[e][41]
[f][42]
[g][43]
[h][44].

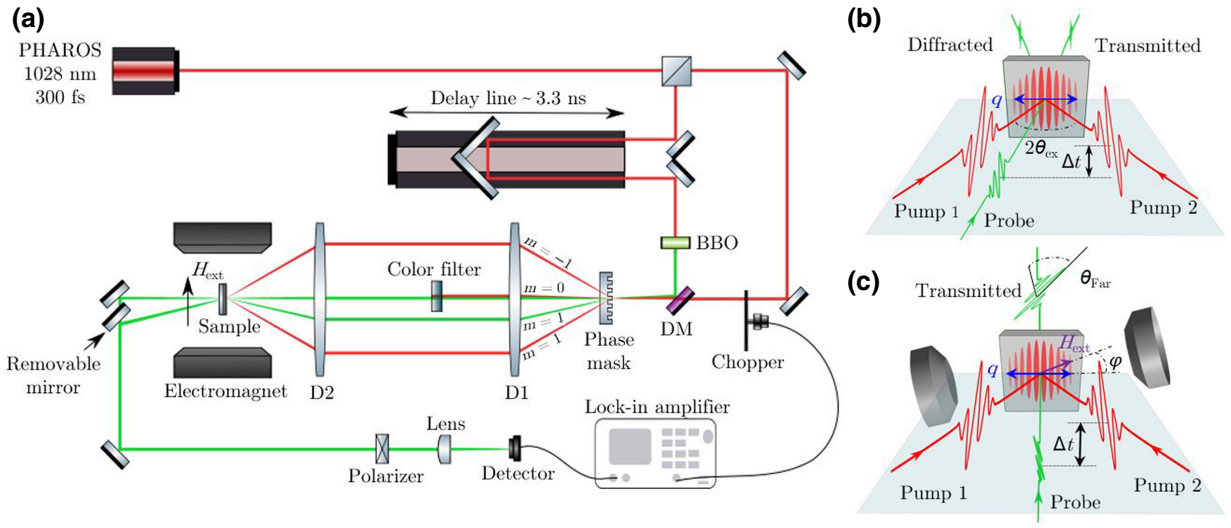

FIG. 1. (a) Scheme of the experimental setup. BBO, β-barium borate crystal for second-harmonic generation; DM, dichroic mirror; D1 and D2, achromatic doublets. (b) Sketch of the TG setup for acoustic measurement. (c) Sketch of the TG setup for magneto-optical Faraday polarimetry.

A key feature of the TG technique is its wave-vector selectivity: the optical grating generated by the pumps has a precise fringe spacing Λ given by phase mask pitch and thus selectively excites phonon modes with wave vector q, obtained with the equation

$$q = \frac{2\pi}{\Lambda} = \frac{4\pi \sin\theta_{ex}}{\lambda_p}, \tag{1}$$

where θ_{ex} and λ_p are, respectively, the half-angle of incidence and the wavelength of the pump beams. For optical wavelengths, q is in the few μm^{-1} range. In a ferromagnetic medium, a SW of equal wavelength and frequency is generated by inverse magnetostriction [29,30]. As from Eq. (1), changing the pumps incidence angle θ_{ex} changes Λ and thus the wave vector of the excited acoustic and spin wave.

To perform TG acoustic spectroscopy in transmission [Fig. 1(b)] we use the $m = 1$ diffraction order of the probe, which impinges off normal on the sample. It is then diffracted by the SAW at the Bragg angle and its intensity modulation at selected time delays with respect to the pumps allows the acquisition of the dynamic information on the relaxing TG, and consequently on the properties of the excited acoustic modes. The diffracted probe is detected with a photoreceiver (Newport Femtowatt 2151) and fed in a lock-in amplifier (SR860), which is phase locked to a mechanical rotating chopper (50% duty cycle, 719 Hz) positioned along the pump path.

An external magnetic field ($\mathbf{H}_{ext}$) is needed when performing SAW FMR [Fig. 1(c)]. We use an electromagnet to generate an in-plane (IP) static magnetic field at an angle $\varphi \approx 15^\circ$ with respect to the SAW wave vector $\mathbf{q}$, as required by symmetry of the magnetoelastic interaction [5]. To detect the TR OOP magnetization dynamics as a function of the applied magnetic field, we perform TR Faraday polarimetry exploiting the 0th order of diffraction of the 514-nm beam as a probe [see Fig. 1(a) and (c)]. The switch from TG acoustic spectroscopy setup to TR Faraday rotation setup can be easily performed by (i) blocking the 0th order of the pump using a color filter, (ii) removing the mirror indicated as *Removable mirror* in Fig. 1(a), and (iii) crossing nearly to extinction the polarizer in the detection branch.

The probe focal spot on the sample is approximately equal to 40 μm in diameter, much larger than the SAW and SW wavelength. This is required for acoustic detection, since diffraction from a grating only happens if several fringes are illuminated; however, it lowers the sensitivity for the magnetic transient, since it allows measurement of only the OOP component of the magnetization, averaged along several wavelengths. Nonetheless, in the TG pumping scheme, the SAW and SW profile is intrinsically entangled to a periodic temperature profile along the **q** direction, due to the stripy pump pattern: as shown in Ref. [7], this ensures that the Faraday rotation signal does not average to zero when integrated along full SW periods, relying on the partial demagnetization of Ni in the illuminated fringes; clearly the Curie temperature of the magnetic thin film is a key parameter to the magneto-optical sensitivity, as shown in detailed simulations [7].

We study polycrystalline Ni films of thickness 14 nm vacuum deposited on (001)-oriented CaF_2 crystalline substrate, and of 8 and 14 nm on amorphous SiO_2 substrate. In all cases, the films are capped with a 10-nm SiO_2 layer to prevent oxidation while ensuring high transmission of

the laser beams. Films and capping layers are deposited by *e*-beam evaporation with a base pressure of 10^{-6} mbar. The magnetostatic properties of the samples are characterized via longitudinal magneto-optical Kerr effect (MOKE) at the NFFA facility (MBE-Cluster) in Trieste, Italy [31]. Further sample characterization can be found within the Supplemental Material [32].

Nickel is often the ferromagnet of choice for magnetoelastic studies, thanks to its high magnetostrictive coefficient ($\lambda_s = -38 \times 10^{-6}$ for a polycrystal [33]). Moreover, the low Curie temperature (628 K, [34]) ensures that the temperature gradients along the SAW wave-vector direction give good contrast in Faraday detection.

The choice of the substrates is guided by Ref. [12]: for thermally generated SAWs, we can define a thermoelastic efficiency η as

$$\eta = \alpha_{\text{th}} \frac{1+\nu}{1-\nu} \frac{1}{c_{\text{th}}}, \tag{2}$$

where α_{th} is the thermal expansion coefficient, ν is the Poisson ratio, and c_{th} is the heat capacity. η is the relevant parameter in quantifying the SAW amplitude for given input thermal stress [32]. Besides the thermoelastic efficiency, the amplitude of the magneto-optical signal is affected by the spatially periodic temperature gradients and the associated magnetization modulation, as pointed out above: thus, as demonstrated in Refs. [7,35], a higher thermal conductivity of the substrate is detrimental for the experiment, since it brings faster thermalization and thus reduced magneto-optical signal. One can define a $\mathcal{F}$ via the following relation:

$$\mathcal{F} = \frac{\eta}{k_{\text{th}}} \tag{3}$$

and seek a specific substrate to maximize $\mathcal{F}$. Table I reports results for some commonly used substrates, including those of our choice. As from Table I, CaF_2 gives a large $\mathcal{F}$; we investigate CaF_2 as a crystalline, high-$\mathcal{F}$ substrate, and SiO_2 as an amorphous, low-$\mathcal{F}$ (about 4 times smaller) substrate. Finally, the transparency in the visible region allows work in transmission geometry.

The broadband FMR experiments are carried out using a homemade setup, where the sample is positioned between the polar extensions of a Bruker ER-200 electromagnet, maintaining its surface parallel to $\mathbf{H}_{\text{ext}}$ in the so-called "flip-chip" configuration for IP measurements. To induce the precession of the magnetization vector, the samples are fixed on a grounded coplanar waveguide, then connected to an Anritsu rf source. The FMR signal for a fixed frequency is acquired by measuring the derivative of the absorption power downstream of the electrical transmission line as a function of H_{ext} through a lock-in amplifier. For further details on the FMR setup, see Ref. [36].

All measurements reported are performed in air and at room temperature.

III. RESULTS AND DISCUSSION

Figure 2 shows MOKE hysteresis loops of the three samples; the reported angles refer to IP azimuth. In Fig. 2(a) the Ni/CaF_2 sample shows a reduction in the absolute value of the magnetic remanence for 0°, indicating a small IP anisotropy not relevant in this context [32]. Differently, Figs. 2(b) and 2(c) display a negligible IP anisotropy and a higher coercive field for the Ni/SiO_2 samples, at fixed thickness. This is in accordance with the amorphous nature of the substrate that favors the growth of less textured Ni films, thus characterized by an isotropic magnetic response.

Figure 3 shows the purely acoustic TG signal of Ni(14 nm)/CaF_2 obtained in transmission geometry with a TG pitch of $\Lambda = 2.5$ μm ($q = 2.47$ μm^{-1}), after subtraction of exponential background. Raw data and details on the background removal procedure can be found within

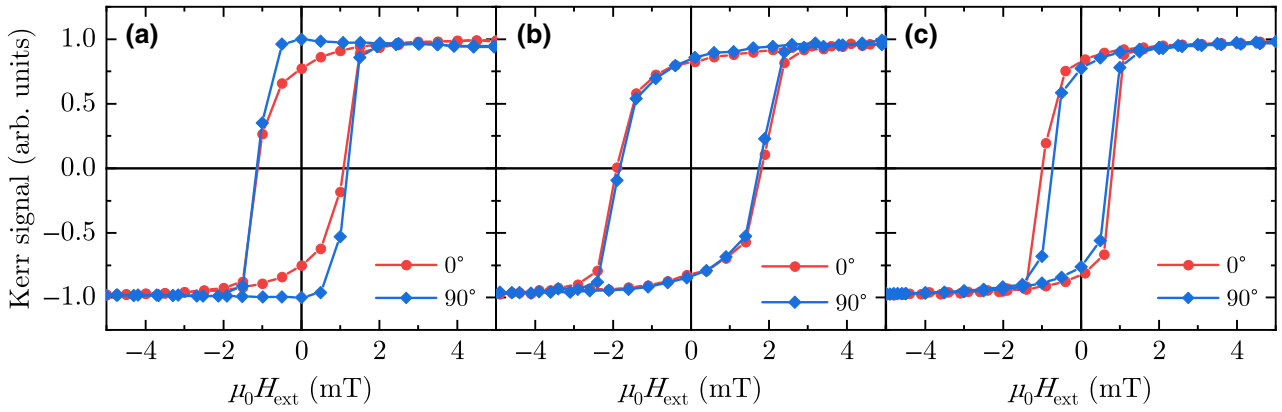

FIG. 2. Hysteresis loops from longitudinal MOKE measurements. The magnetic field is applied IP; the angles refer to azimuth. (a) Ni(14 nm)/CaF_2 sample. The 0° orientation is defined by the IP magnetic field being along the [100] crystallographic direction of the substrate. (b) Ni(14 nm)/SiO_2. (c) Ni(8 nm)/SiO_2. In (b) and (c) the IP angles are measured from an arbitrary edge of the sample.

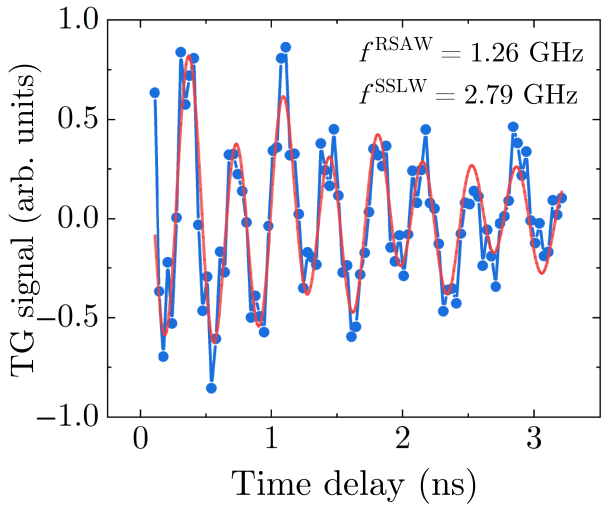

FIG. 3. Ni(14 nm)/CaF_2 acoustic TG signal after subtraction of exponential background (blue dots). The trace is obtained with a pitch $\Lambda = 2.5$ μm. No magnetic field is applied. Time-domain fit (red solid line) of Eq. (4) gives the frequency of the SSLW (2.79 GHz) and RSAW (1.26 GHz).

the Supplemental Material [32]. A satisfactory fit of the observed intensity (I) oscillations requires two sines:

$$I = A_1 \sin(2\pi f_1 t + \phi_1) + A_2 \sin(2\pi f_2 t + \phi_2) + B, \quad (4)$$

from which we obtain $f_1 = 1.26 \pm 0.06$ GHz and $f_2 = 2.79 \pm 0.02$ GHz, corresponding, respectively, to the Rayleigh surface acoustic wave (RSAW) and the surface skimming longitudinal wave (SSLW), in agreement with previous studies [7]; the phase velocities ($c = 2\pi f\,/q$) are $c_{RSAW} = 3.2 \pm 0.2$ km/s and $c_{SSLW} = 7.1 \pm 0.05$ km/s.

The presence of magnetoelastic coupling (magnetostriction, piezomagnetism, or higher-order terms) allows exploitation of time-varying acoustic fields (e.g., SAWs with Λ at the micron scale) as an effective rf magnetic field; in this work we apply this SAW-driven FMR method. The azimuthal angle φ between $\mathbf{q}$ and $\mathbf{H}_{ext}$ is a critical parameter for the strength of the magnetoelastic coupling [5,6,10]. The nonuniform tickle magnetoelastic field produces a nonuniform magnetization precession, i.e., a finite-wave-vector SW [30].

The dynamics of the magnetization $\mathbf{M}$ of a ferromagnet is generally described with the Landau-Lifshitz-Gilbert equation [45]

$$\frac{d\mathbf{M}}{dt} = -\gamma \mathbf{M} \times \mu_0 \mathbf{H}_{eff} + \frac{\alpha}{M}\left(\mathbf{M} \times \frac{d\mathbf{M}}{dt}\right), \quad (5)$$

where μ_0 is the vacuum magnetic permeability, γ is the gyromagnetic ratio, $\alpha > 0$ is the so-called Gilbert-damping parameter, and $\mathbf{H}_{eff}$ is the effective field, which includes $\mathbf{H}_{ext}$ and all other internal fields (e.g., anisotropy, demagnetizing). The Larmor precession of $\mathbf{M}$ about $\mathbf{H}_{eff}$ [first term at right-hand side of Eq. (5)] has angular frequency $\omega_L = \gamma \mu_0 H_{eff}$ typically in the GHz range. Dissipation of energy and of angular momentum towards other degrees of freedom of the material or to free space (second term) leads to the alignment of $\mathbf{M}$ along the $\mathbf{H}_{eff}$ axis.

The FMR condition is reached by adding a rf magnetic field at frequency ω_L to compensate the damping, so that $\mathbf{M}$ can be set in stable precession. No restrictions are imposed to the nature of the rf field. The analytical dependence of the FMR frequency f strongly depends on the strength of the applied magnetic field and on the shape of the sample. In the case of a thin isotropic ferromagnetic film under IP magnetic field, f is given by the Kittel formula [46,47]

$$f = \frac{\mu_0 \gamma}{2\pi}\sqrt{H_{eff}^{res}\left(H_{eff}^{res} + M_{eff}\right)}, \quad (6)$$

where H_{eff}^{res} is the value of the effective field at resonance condition and M_{eff} is the effective magnetization of the sample, which is related to the saturation magnetization M_s via $M_{eff} = M_s - 2K_s/M_s d_{FM}$: here K_s is the surface anisotropy constant and d_{FM} is the thickness of the ferromagnetic thin film [48,49].

Figure 4 reports SAW FMR results obtained on Ni(14 nm)/CaF_2 with TG pitch $\Lambda = 2.5$ μm, with SAW wave vector $\mathbf{q}$ along the [100] direction of the substrate; in all these measurements, $\mathbf{H}_{ext}$ is applied IP at angle $\varphi \approx 15°$. Panel (a) shows the intensity of the TR Faraday signal as a function of the time delay between the pump and probe at two applied magnetic fields (23.3 and 5.4 mT, blue dots and red diamonds, respectively). The periodicity of the signal is highly influenced by the applied field. A systematic investigation of this effect is shown in (b) where a two-dimensional (2D) map of the TR Faraday signal is reported versus time delay and versus magnetic field. The strong dependence of periodicity and amplitude of the TR Faraday signal is indeed due to SAW FMR. Panel (c) reports the FFT of (b): clear resonances are visible where $H_{eff} = H_{res}$, such that the Kittel frequency matches either the RSAW or the SSLW frequency. Similar maps are acquired with TG pitches $\Lambda = 3$ and 4 μm. A change of Λ corresponds to a change of the RSAW and SSLW frequency, along the linear dispersion relation of acoustic modes: hence, SAW FMR resonances can be tuned at the desired frequency and magnetic field.

We then combine the FFT maps obtained with the three different TG pitches ($\Lambda = 2.5$, 3, and 4 μm) to extract the SAW FMR parameters, namely the frequency and magnetic field in resonance condition. For each TG pitch, we exploit the symmetry in the applied magnetic field by folding the FFT maps around the zero field to obtain better contrast [35]; note that any hysteretic behavior is averaged out by this procedure. From the three folded maps, we extract the SAW FMR resonance frequency by integrating over a suitable range of magnetic field and

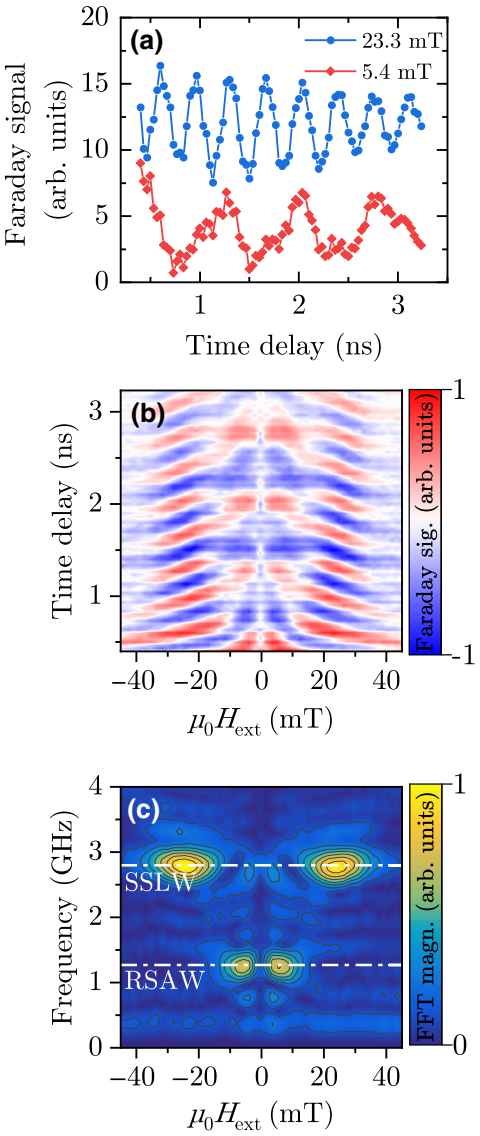

FIG. 4. (a) TR Faraday traces from Ni(14 nm)/CaF_2 at resonance with SSLW (blue dots, $\mu_0 H_{ext} = 23.3$ mT) and RSAW (red diamonds, $\mu_0 H_{ext} = 5.4$ mT), with $\Lambda = 2.5$ μm. After subtraction of linear background, the traces are vertically offset for clarity. (b) 2D map of the Faraday signal intensity as a function of time delay and applied magnetic field. Each trace has been normalized to its maximum after linear background subtraction. (c) 2D FFT magnitude map of each trace in (b). The dash-dot red lines at 1.26 and 2.79 GHz correspond to the frequency, respectively, of the RSAW and SSLW [Fig. 3(b)], identifying magnetoelastically enhanced magnetization precession.

fitting the obtained curve with a Gaussian to extract the peak frequency; similarly, by integrating over a suitable range of frequencies, we determine the resonance magnetic field and its linewidth, identified as the peak position and FWHM of the fitting curve, respectively.

Comparison between standard FMR and SAW FMR is presented in Fig. 5(a), for the case of IP magnetic field: $\mathbf{H}_{ext}$ is assumed to be uniform for both configurations and, together with the magnetic shape anisotropy, determines the equilibrium axis of $\mathbf{M}$. In standard FMR a rf wave is applied to the sample to have its oscillating magnetic component $\mathbf{H}_{rf}$ orthogonal to $\mathbf{H}_{eff}$, exciting the precession of the $\mathbf{M}$ vector [panel (a), top] [50,51]. In SAW FMR [panel (a), bottom], the rf field is generated by an elastic wave (the red stripes represent the SAW wave fronts).

Panels (b),(c) in Fig. 5 compare results of standard FMR and SAW FMR from the very same sample of Ni(14 nm)/CaF_2. The resonance frequency obtained with both techniques as a function of the magnetic field is reported in (b), together with fits of the Kittel curve [Eq. (6)]. In the fit of standard FMR data, both γ and M_{eff} are free parameters: the best fit is obtained for $\gamma = (2.10 \pm 0.06) \times 10^{11}$ rad/s T and $M_{eff} = 199 \pm 18$ kA/m. Due to the limited SAW FMR dataset, when fitting it we fix $\gamma = 2.10 \times 10^{11}$ rad s T; we obtain $M_{eff} = 195 \pm 16$ kA/m, in perfect agreement with what we find from the FMR data. The low M_{eff} values with respect to the saturation magnetization of Ni at room temperature ($M_{sat} \approx 490$ kA/m, [34]) are attributed to a growth-induced IP anisotropy and possible impurities introduced during sample deposition. Indeed, M_{eff} strongly depends also on the ferromagnetic thickness, even above the ultrathin regime, as reported, e.g., in Ref. [36] and the Supplemental Material therein. Furthermore, the fully consistent M_{eff} values suggest that in both techniques the sample can be considered at room temperature, which indirectly means that the TG-induced temperature profile does not affect the magnetic properties of the sample significantly.

We stress that the magnetization precession is uniform in FMR and nonuniform in SAW FMR: the latter could be thus thought as a SW resonance technique, and it is in principle not obvious that a Kittel curve should appear, as in the small $\mathbf{q}$ range the SW dispersion relation can have huge nonmonotonous dependence due to dipolar fields (backward volume magnetostatic waves, BVMSWs, see, e.g., Refs. [52,53]). Nevertheless, for the specific case we address in this work, it can be shown that the contribution of BVMSW is negligible and the dispersion relation of SWs in the wave-vector range of our interest is flat within 10% [32,54]. This means that we can directly compare our results to FMR, and we can properly call the projected curve a "Kittel curve." We do not include any uniaxial anisotropy term, which could arise from the thermally induced static and dynamic surface rippled pattern, which is in the micron range in our experiment [55]: indeed, this anisotropy is known to be negligible for ripple wavelength larger than about 100 nm [56,57].

The linewidth ΔH_{FWHM} of the resonance acquired with FMR and SAW FMR is reported in Fig. 5(c). For FMR, the linewidth is the FWHM in a sweep of H_{ext}. To compare the FMR and SAW FMR linewidths, the FWHM value extracted from the SAW FMR signal along the magnetic

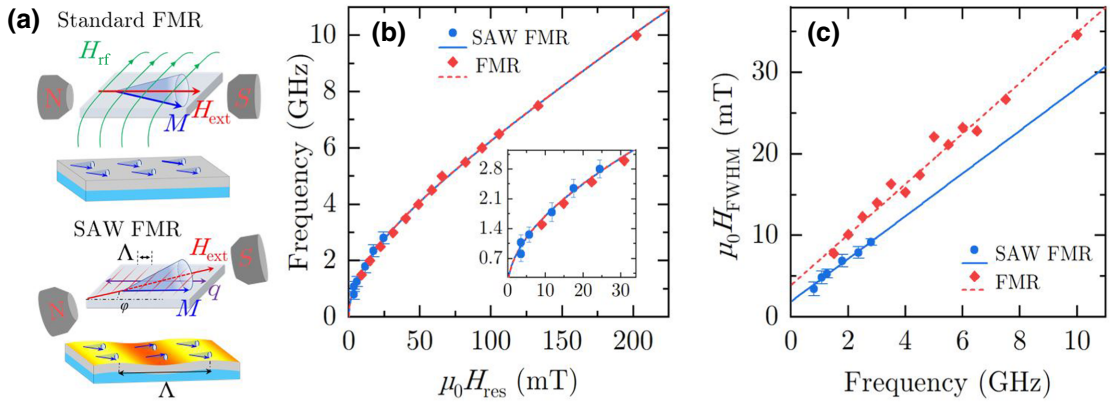

FIG. 5. (a) Top: geometry and scheme of standard FMR. The magnetization precesses uniformly over the entire sample. Bottom: geometry and scheme of SAW FMR. The magnetization traces a cone about $\mathbf{H}_{\text{eff}}$ in a nonuniform mode, following the space and time modulation of the SAW strain field. (b) SAW FMR (blue dots) and standard FMR (red diamonds) measurements with the applied magnetic field along the [100] direction. The lines (blue solid for FMR and red dashed for SAW FMR) are the fits with the Kittel formula [Eq. (6)]. (c) Magnetic field FWHM as a function of the resonance frequency. The lines are linear fits [Eq. (7)]. The error bars in the FMR data in (b),(c) are smaller than the marker size.

field axis of the magnitude of FFT is divided by $\sqrt{3}$: this factor is needed (as can be derived from Ref. [29]) since we work with the magnitude of the FFT rather than with the imaginary part. Following standard analysis from FMR [48,58], we extract the Gilbert damping α by fitting the linewidths with the equation

$$\Delta H_{\text{FWHM}} = \frac{4\pi\alpha}{\gamma} f + \Delta H_{\text{inh}}, \tag{7}$$

where ΔH_{inh} is the so-called homogeneous broadening term, which is a frequency-independent line broadening due to magnetostructural disorder [48]. For SAW FMR we obtain $\alpha = (47 \pm 5) \times 10^{-3}$ and $\Delta H_{\text{inh}} = 1.8 \pm 0.5$ mT, again in good agreement with the values obtained from FMR, namely $\alpha = (52 \pm 2) \times 10^{-3}$ and $\Delta H_{\text{inh}} = 3.9 \pm 0.4$ mT. We attribute the somewhat larger ΔH_{inh} from FMR to large-scale inhomogeneities that contribute to the FMR signal, as FMR is an area-integrated technique.

An overview of the SAW FMR approach is given in Fig. 6, showing the experimental data (black spheres) of the Ni(14 nm)/CaF_2 in a three-dimensional (3D) phase space spanned by the magnetoelastic resonance frequency f, the SAW wave vector q, and the resonance magnetic field H_{res}. Three wave vectors q (1.57, 2.05, and 2.47 μm^{-1}) are identified with vertical planes (orange, light blue, and purple, respectively). Two acoustic modes are at play, namely RSAW and SSLW. At fixed q, the sound velocity of each SAW determines the two frequencies: thus the projection onto the (f, q) plane (green dots) gives the linear acoustic dispersion for the two modes (linear fit in pink). Given the flatness of the SW dispersion in the range of interest, the projection onto the (f, H_{res}) plane (blue dots) can be fitted with a Kittel curve [in red, see Eq. (6)].

From Fig. 4(c), H_{ext} is understood as the driving parameter to obtain SAW FMR: indeed, tuning H_{ext} makes the SW manifold move in the phase space of Fig. 6, while the SAW dispersions are not affected; the elastic and magnetic degrees of freedom couple resonantly when frequency and wave vector of a SW match those of a SAW. It is worth noting the great potentiality of SAW FMR to investigate nonflat SW dispersions, extending the FMR measurement along the q axis: this will be of interest, e.g., for addressing specific momentum-dependent damping channels, such as two-magnon scattering (TMS) phenomena [59–64].

Having ascertained the capabilities and the reference frame of the TG SAW FMR experiments in comparison with standard FMR, we now quantify the sensitivity of the

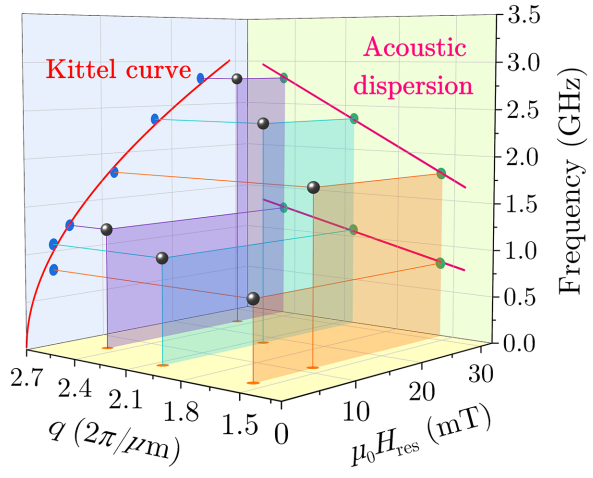

FIG. 6. 3D phase space of TG measurements on the 14-nm Ni/CaF_2 film. The black spheres are experimental points corresponding to SAW FMR resonance conditions.

technique by presenting data from samples with low $\mathcal{F}$, namely Ni films (14 and 8 nm) on fused silica (see Table I). In Fig. 7(a)–(c), FFT maps at different Λ are reported: compared to Fig. 4(c), additional reference lines highlight higher-order resonance peaks parametrically excited at a half multiple or at a combination of the two SAW frequencies [26]. Several parametric resonances are visible from Ni(14 nm), while from Ni(8 nm) a single parametric resonance is observed (not shown). The observation of such higher-order resonances testifies the sensitivity of the detection scheme and the capability of TG-based acoustic excitation to drive large amplitude magnetic precession.

Following the same procedure described above, we extract M_{eff} and α for the Ni(14 nm)/SiO_2 and Ni(8 nm)/SiO_2 samples. Figure 7(d) reports f as a function of H_{res}, showing that also the parametric resonances follow the Kittel curve. The low-frequency cutoff in Ni(14 nm) in Fig. 7(d) (blue squares) resembles what is observed in high-frequency magnetoimpedance measurements [65], where the frequency border from quasistatic to resonating precession is crossed. Such a cutoff is observed in Ni(14 nm) at applied magnetic field close to the opening of the hysteresis loop [see Fig. 2(b)]: we speculate it to be due to loss of magnetic saturation and formation of magnetic domains, a hypothesis consistent with the absence of such a cutoff in Ni(8 nm)/SiO_2 and in Ni(14 nm)/CaF_2, whose hystereses are narrower, thus maintaining the sample in equilibrium condition. We exclude from the fit unsaturated data, i.e., Ni(14 nm) data (either parametric or not) with $f \leq 1$ GHz and we fix $\gamma = 1.93 \times 10^{11}$ rad/s T. Such a value of γ is obtained from FMR measurement on a similar sample. We obtain $M_{\text{eff}} = 277 \pm 16$ kA/m for Ni(14 nm)/SiO_2 and $M_{\text{eff}} = 122 \pm 16$ kA/m for Ni(8 nm)/SiO_2. Also in this case, the reduction of the Ni thickness is accompanied by a reduction of the M_{eff} value, in accordance with [36]. The different M_{eff} values observed for the Ni(14 nm)/SiO_2 and Ni(14 nm)/CaF_2 samples are explained in terms of the structural and morphological properties induced by the substrate during the Ni growth, which promotes a different texturization of the Ni crystalline grains [32].

Figure 7(e) shows ΔH_{FWHM} as a function of f. By fitting with Eq. (7) we obtain $\alpha = 0.11 \pm 0.01$ and $\alpha = 0.12 \pm 0.04$ for Ni(14 nm) and Ni(8 nm), respectively; ΔH_{inh} is compatible with zero for both samples. Again, Ni(14 nm) and Ni(8 nm) data marked as squares and stars, respectively, are excluded from the fit in order to limit spurious enhancement of α due to incomplete magnetic saturation.

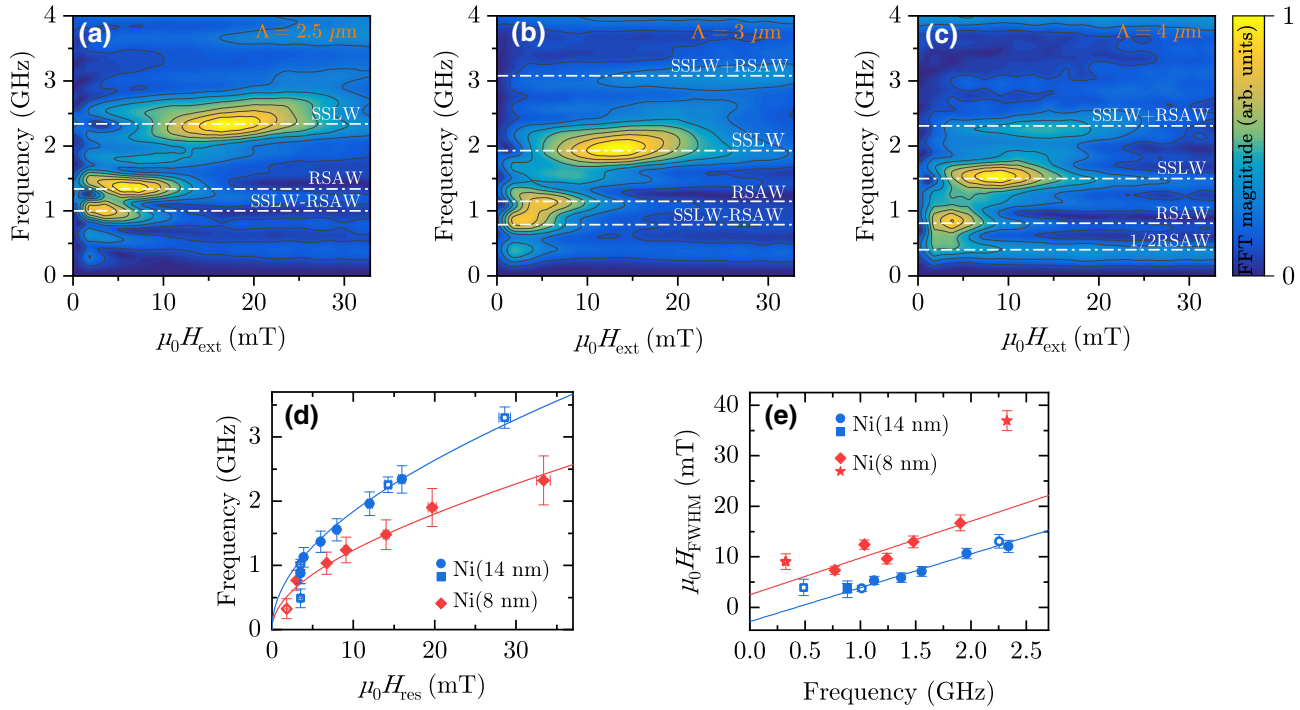

FIG. 7. (a)–(c) 2D FFT magnitude map of the TR Faraday signals from Ni(14 nm)/SiO_2 for $\Lambda = 2.5$, 3, and 4 μm. The dash-dot white lines highlight the frequencies of the TG-pumped acoustic modes and the additional parametric frequencies. (d) SAW FMR results from Ni(14 nm)/SiO_2 (blue dots) and Ni(8 nm)/SiO_2 (red diamonds). Data excluded from the fits are plotted as blue squares and red stars for Ni(14 nm) and Ni(8 nm), respectively. Empty markers denote parametric resonances. Frequency error bars are the FWHM along the frequency axis of the FFT peaks, while the error on the applied magnetic field is estimated approximately equal to 5%. The solid lines are the fits with the Kittel formula [Eq. (6)]. (e) Magnetic field FWHM as a function of the resonance frequency. The marker legenda is the same as in (d). Solid lines are linear fits [Eq. (7)].

Such large values for α can be due to growth-induced magnetostructural disorder [36]: as reported in Ref. [66], the substrate can dramatically affect the FMR response of an ultrathin ferromagnetic overlayer; intercalation of a smooth buffer layer improves the film growth as well as the FMR signal. Measurements on a wider range of q would definitely help to clarify the role of parametric resonances in the magnetization dynamics and its damping as well as to determine ΔH_{inh}.

IV. CONCLUSIONS

In summary, we perform SAW FMR on polycrystalline Ni thin films, combining TG-based excitation of SAWs and TR Faraday polarimetry on the magnetoelastically induced magnetic precession. The close comparison of results from SAW FMR and standard FMR, performed on the very same sample, establishes the validity of SAW FMR as a method for magnetic and magnetoelastic characterization. The high space resolution of our experimental setup, only limited by the laser focal spot and the SAW wavelength, allows the study of local magnetization dynamic properties of magnetic systems, a condition not achievable using area-integrated techniques (e.g., FMR).

Momentum-dependent time-resolved scattering techniques are needed to investigate complex quantum systems and devices, with special emphases on the decay channels of low-energy excitations (phonons, magnons . . .). The wave-vector selectivity of the presented technique can be fruitfully employed in addressing the Gilbert damping in transition metal and magnetic oxide thin films with nonmonotonous SW dispersion [60]. In these systems, TMS is understood as a major dissipation channel, and its cross section is largely affected by inhomogeneities of the magnetic landscape and by their typical length scale. In this respect, a TR and wave-vector-selective technique provides a direct insight into the decay mechanisms. Furthermore, Dzyaloshinskii-Moriya interaction (DMI) is known to have a large impact on the SW dispersion and on the symmetry of the magnetoelastic coupling (nonreciprocity [67]). The study of transition metal/heavy metal magnetic multilayers and of chiral magnets where DMI and/or interfacial DMI are at play can largely benefit from a TG-based and magnetization-sensitive technique. These systems possibly host a skyrmion phase: the TG method combined with a magnetic probe could also be an efficient way to investigate the optical generation of acoustically driven skyrmions [68], together with their time-resolved dynamics.

ACKNOWLEDGMENTS

The authors thank A. Fondacaro, F. Salvador, and D. Benedetti for their technical support. G.P. thanks C.H. Back for valuable suggestions. This work is performed in the framework of the Nanoscience Foundry and Fine Analysis (NFFA-MUR Italy Progetti Internazionali) facility, and in the EU's H2020 framework programme for research and innovation NFFA-Europe-Pilot under Grant Agreement No. 101007417.

[1] J. F. Gregg, I. Petej, E. Jouguelet, and C. Dennis, Spin electronics—A review, J. Phys. D: Appl. Phys. **35**, R121 (2002).

[2] A. V. Chumak, A. A. Serga, and B. Hillebrands, Magnonic crystals for data processing, J. Phys. D: Appl. Phys. **50**, 244001 (2017).

[3] P. Pirro, V. I. Vasyuchka, A. A. Serga, and B. Hillebrands, Advances in coherent magnonics, Nat. Rev. Mater. **6**, 1114 (2021).

[4] W. G. Yang and H. R. Schmidt, Acoustic control of magnetism toward energy-efficient applications, Appl. Phys. Rev. **8**, 021304 (2021).

[5] M. Weiler, L. Dreher, C. Heeg, H. Huebl, R. Gross, M. S. Brandt, and S. T. B. Gönnenwein, Elastically Driven Ferromagnetic Resonance in Nickel Thin Films, Phys. Rev. Lett. **106**, 117601 (2011).

[6] L. Dreher, M. Weiler, M. Pernpeintner, H. Huebl, R. Gross, M. S. Brandt, and S. T. B. Gönnenwein, Surface acoustic wave driven ferromagnetic resonance in nickel thin films: Theory and experiment, Phys. Rev. B **86**, 134415 (2012).

[7] J. Janušonis, T. Jansma, C. L. Chang, Q. Liu, A. Gatilova, A. M. Lomonosov, V. Shalagatskyi, T. Pezeril, V. V. Temnov, and R. I. Tobey, Transient grating spectroscopy in magnetic thin films: Simultaneous detection of elastic and magnetic dynamics, Sci. Rep. **6**, 1 (2016).

[8] P. Kuszewski, J.-Y. Duquesne, L. Becerra, A. Lemaître, S. Vincent, S. Majrab, F. Margaillan, C. Gourdon, and L. Thevenard, Optical Probing of Rayleigh Wave Driven Magnetoacoustic Resonance, Phys. Rev. Appl. **10**, 034036 (2018).

[9] V. Polewczyk, K. Dumesnil, D. Lacour, M. Moutaouekkil, H. Mjahed, N. Tiercelin, S. P. Watelot, H. Mishra, Y. Dusch, and S. Hage-Ali, *et al.*, Unipolar and Bipolar High-Magnetic-Field Sensors Based on Surface Acoustic Wave Resonators, Phys. Rev. Appl. **8**, 024001 (2017).

[10] P. G. Gowtham, T. Moriyama, D. C. Ralph, and R. A. Buhrman, Traveling surface spin-wave resonance spectroscopy using surface acoustic waves, J. Appl. Phys. **118**, 233910 (2015).

[11] J. Janušonis, C. L. Chang, P. H. M. van Loosdrecht, and R. I. Tobey, Frequency tunable surface magneto elastic waves, Appl. Phys. Lett. **106**, 181601 (2015).

[12] H. J. Eichler, P. Günter, and D. W. Pohl, *Laser-Induced Dynamic Gratings* (Springer Berlin, Heidelberg, 1986).

[13] Y.-X. Yan and K. A. Nelson, Impulsive stimulated light scattering. I. General theory, J. Chem. Phys. **87**, 6240 (1987).

[14] L. Dhar, J. A. Rogers, and K. A. Nelson, Time-resolved vibrational spectroscopy in the impulsive limit, Chem. Rev. **94**, 157 (1994).

[15] J. A. Rogers, A. A. Maznev, M. J. Banet, and K. A. Nelson, Optical generation and characterization of acoustic waves

in thin films: Fundamentals and applications, Ann. Rev. Mater. Sci. **30**, 117 (2000).
[16] N. Gedik, J. Orenstein, R. Liang, D. A. Bonn, and W. N. Hardy, Diffusion of nonequilibrium quasi-particles in a cuprate superconductor, Science **300**, 1410 (2003).
[17] R. Torre, *Time-Resolved Spectroscopy in Complex Liquids* (Springer New York, New York, 2007).
[18] R. Cucini, A. Taschin, P. Bartolini, and R. Torre, Acoustic, thermal and flow processes in a water filled nanoporous glass by time-resolved optical spectroscopy, J. Mech. Phys. Solids **58**, 1302 (2010).
[19] M. Sander, M. Herzog, J. E. Pudell, M. Bargheer, N. Weinkauf, M. Pedersen, G. Newby, J. Sellmann, J. Schwarzkopf, and V. Besse, *et al.*, Spatiotemporal Coherent Control of Thermal Excitations in Solid, Phys. Rev. Lett. **119**, 075901 (2017).
[20] J. R. Rouxel, D. Fainozzi, R. Mankowsky, B. Rösner, G. Seniutinas, R. Mincigrucci, S. Catalini, L. Foglia, R. Cucini, and F. Döring, *et al.*, Hard x-ray transient grating spectroscopy on bismuth germanate, Nat. Photonics **15**, 499 (2021).
[21] C. L. Chang, S. Mieszczak, M. Zelent, V. Besse, U. Martens, R. R. Tamming, J. Janusonis, P. Graczyk, M. Münzenberg, and J. W. Kłos, *et al.*, Driving Magnetization Dynamics in an On-Demand Magnonic Crystal via the Magnetoelastic Interactions, Phys. Rev. Appl. **10**, 064051 (2018).
[22] D. Weder, C. von Korff Schmising, C. M. Günther, M. Schneider, D. Engel, P. Hessing, C. Strüber, M. Weigand, B. Vodungbo, and E. Jal, *et al.*, Transient magnetic gratings on the nanometer scale, Struct. Dyn. **7**, 054501 (2020).
[23] D. Ksenzov, A. A. Maznev, V. Unikandanunni, F. Bencivenga, F. Capotondi, A. Caretta, L. Foglia, M. Malvestuto, C. Masciovecchio, and R. Mincigrucci, *et al.*, Nanoscale transient magnetization gratings created and probed by femtosecond extreme ultraviolet pulses, Nano Lett. **27**, 2905 (2021).
[24] K. Yao, F. Steinbach, M. Borchert, D. Schick, D. Engel, F. Bencivenga, R. Mincigrucci, L. Foglia, E. Pedersoli, and D. De Angelis, *et al.*, All-optical switching on the nanometer scale excited and probed with femtosecond extreme ultraviolet pulses, Nano Lett. **22**, 4452 (2022).
[25] C. L. Chang, Ph.D. Thesis, University of Groningen, 2019.
[26] C. L. Chang, A. M. Lomonosov, J. Janušonis, V. S. Vlasov, V. V. Temnov, and R. I. Tobey, Parametric frequency mixing in a magnetoelastically driven linear ferromagnetic-resonance oscillator, Phys. Rev. B **95**, 060409 (2017).
[27] R. Cucini, T. Pincelli, G. Panaccione, D. Kopic, F. Frassetto, P. Miotti, G. M. Pierantozzi, S. Peli, A. Fondacaro, and A. De Luisa, *et al.*, Coherent narrowband light source for ultrafast photoelectron spectroscopy in the 17–31 ev photon energy range, Struct. Dyn. **7**, 014303 (2020).
[28] A. A. Maznev, T. F. Crimmins, and K. A. Nelson, How to make femtosecond pulses overlap, Opt. Lett. **23**, 1378 (1998).
[29] A. G. Gurevich and G. A. Melkov, *Magnetization Oscillations and Waves* (CRC Press, London, 2020).
[30] B. Casals, N. Statuto, M. Foerster, A. Hernández-Mínguez, R. Cichelero, P. Manshausen, A. Mandziak, L. Aballe, J. M. Hernàndez, and F. Macià, Generation and Imaging of Magnetoacoustic Waves over Millimeter Distances, Phys. Rev. Lett. **124**, 137202 (2020).
[31] G. Vinai, F. Motti, A. Y. Petrov, V. Polewczyk, V. Bonanni, R. Edla, B. Gobaut, J. Fujii, F. Suran, and D. Benedetti, *et al.*, An integrated ultra-high vacuum apparatus for growth and in situ characterization of complex materials, Rev. Sci. Instrum. **91**, 085109 (2020).
[32] See Supplemental Material at http://link.aps.org/supplemental/10.1103/PhysRevApplied.18.044009 for further sample characterization, discussion on magnetic anisotropy, and details on data analysis, thermoelastic efficiency modeling, and spin-wave dispersion..
[33] E. Klokholm and J. Aboaf, The saturation magnetostriction of thin polycrystalline films of iron, cobalt, and nickel, J. Appl. Phys. **53**, 2661 (1982).
[34] J. M. D. Coey, *Magnetism and Magnetic Materials* (Cambridge University Press, New York, 2010).
[35] J. Janušonis, C.-L. Chang, T. Jansma, A. Gatilova, V. S. Vlasov, A. M. Lomonosov, V. V. Temnov, and R. I. Tobey, Ultrafast magnetoelastic probing of surface acoustic transients, Phys. Rev. B **94**, 024415 (2016).
[36] E. Longo, M. Belli, M. Alia, M. Rimoldi, R. Cecchini, M. Longo, C. Wiemer, L. Locatelli, P. Tsipas, and A. Dimoulas, *et al.*, Large spin-to-charge conversion at room temperature in extended epitaxial Sb_2Te_3 topological insulator chemically grown on silicon, Adv. Funct. Mat. **32**, 2109361 (2022).
[37] https://www.opticalsolutions.it/en/defence-ir-components-en/caf2-en/calcium-fluoride-caf2/.
[38] https://www.azom.com/article.aspx?ArticleID=52.
[39] https://www.azom.com/article.aspx?ArticleID=2362.
[40] S. Benyettou, First principles study of the structural, elastic and thermodynamic properties of the cubic perovskite-type SrTiO3, Model. Meas. Contr. **B**, 87 (2018).
[41] https://www.azom.com/properties.aspx?ArticleID=54.
[42] https://www.azom.com/properties.aspx?ArticleID=1387.
[43] T. P. Seward and T. Vascott, *High Temperature Glass Melt Property Database for Process Modeling* (The American Ceramic Society, Westerville, 2005).
[44] https://www.azom.com/properties.aspx?ArticleID=599.
[45] J. Stöhr and H. C. Siegmann, *Magnetism* (Springer Berlin, Heidelberg, 2006).
[46] C. Kittel, On the theory of ferromagnetic resonance absorption, Phys. Rev. **73**, 155 (1948).
[47] C. Kittel and P. McEuen, *Kittel's Introduction to Solid State Physics* (John Wiley & Sons, Hoboken NW, 2018).
[48] S. Azzawi, A. T. Hindmarch, and D. Atkinson, Magnetic damping phenomena in ferromagnetic thin-films and multilayers, J. Phys. D: Appl. Phys. **50**, 473001 (2017).
[49] E. Longo, C. Wiemer, M. Belli, R. Cecchini, M. Longo, M. Cantoni, C. Rinaldi, M. D. Overbeek, C. H. Winter, and G. Gubbiotti, *et al.*, Ferromagnetic resonance of Co thin films grown by atomic layer deposition on the Sb_2Te_3 topological insulator, J. Magn. Magn. Mat. **509**, 166885 (2020).
[50] M. Farle, Ferromagnetic resonance of ultrathin metallic layers, Rep. Prog. Phys. **61**, 755 (1998).
[51] S. S. Kalarickal, P. Krivosik, M. Wu, C. E. Patton, M. L. Schneider, P. Kabos, T. J. Silva, and J. P. Nibarger, Ferromagnetic resonance linewidth in metallic thin films:

Comparison of measurement methods, J. Appl. Phys. **99**, 093909 (2006).
[52] A. Prabhakar and D. D. Stancil, *Spin Waves: Theory and Applications* (Springer New York, New York, 2009).
[53] C. E. Patton, Magnetic excitations in solids, Phys. Rep. **103**, 251 (1984).
[54] B. A. Kalinikos, Spectrum and linear excitation of spin waves in ferromagnetic films, Sov. Phys. J. **24**, 718 (1981).
[55] U. Choudhry, T. Kim, M. Adams, J. Ranasinghe, R. Yang, and B. Liao, Characterizing microscale energy transport in materials with transient grating spectroscopy, J. Appl. Phys. **130**, 231101 (2021).
[56] J. Fassbender, T. Strache, M. O. Liedke, D. Markó, S. Wintz, K. Lenz, A. Keller, S. Facsko, I. Mönch, and J. McCord, Introducing artificial length scales to tailor magnetic properties, New J. Phys. **11**, 125002 (2009).
[57] S. K. Vayalil, A. Koorikkat, A. K. Gopi, S. V. Roth, and P. S. A. Kumar, Tailoring of uniaxial magnetic anisotropy in permalloy thin films using nanorippled Si substrates, J. Phys. Condens. Matter **32**, 185804 (2020).
[58] T. D. Rossing, Resonance linewidth and anisotropy variation in thin films, J. Appl. Phys. **34**, 995 (1963).
[59] M. J. Hurben and C. E. Patton, Theory of two magnon scattering microwave relaxation and ferromagnetic resonance linewidth in magnetic thin films, J. Appl. Phys. **83**, 4344 (1998).
[60] G. Woltersdorf, M. Buess, B. Heinrich, and C. H. Back, Time Resolved Magnetization Dynamics of Ultrathin Fe (001) Films: Spin-pumping and Two-Magnon Scattering, Phys. Rev. Lett. **95**, 037401 (2005).
[61] S. S. Kalarickal, N. Mo, P. Krivosik, and C. E. Patton, Ferromagnetic resonance linewidth mechanisms in polycrystalline ferrites: Role of grain-to-grain and grain-boundary two-magnon scattering processes, Phys. Rev. B **79**, 094427 (2009).
[62] I. Barsukov, F. M. Römer, R. Meckenstock, K. Lenz, J. Lindner, A. Banholzer, M. Körner, J. Grebing, J. Fassbender, and M. Farle, *et al.*, Frequency dependence of spin relaxation in periodic systems, Phys. Rev. B **84**, 140410 (2011).
[63] M. Körner, K. Lenz, R. A. Gallardo, M. Fritzsche, A. Mücklich, S. Facsko, J. Lindner, P. Landeros, and J. Fassbender, Two-magnon scattering in permalloy thin films due to rippled substrates, Phys. Rev. B **88**, 054405 (2013).
[64] L. J. Atkinson, T. A. Ostler, O. Hovorka, K. K. Wang, B. Lu, G. P. Ju, J. Hohlfeld, B. Bergman, B. Koopmans, and R. W. Chantrell, Effects of interactions on the relaxation processes in magnetic nanostructures, Phys. Rev. B **94**, 134431 (2016).
[65] D. De Cos, A. Garcia-Arribas, and J. M. Barandiaran, Ferromagnetic resonance in gigahertz magneto-impedance of multilayer systems, J. Magn. Magn. Mater. **304**, 218 (2006).
[66] S. Yoshii, R.O. Ohshima, Y. Ando, T. Shinjo, and M. Shiraishi, Detection of ferromagnetic resonance from 1 nm-thick Co, Sci. Rep. **10**, 1 (2020).
[67] M. Küß, M. Heigl, L. Flacke, A. Hörner, M. Weiler, M. Albrecht, and A. Wixforth, Nonreciprocal Dzyaloshinskii–Moriya Magnetoacoustic Waves, Phys. Rev. Lett. **125**, 217203 (2020).
[68] T. Yokouchi, S. Sugimoto, B. Rana, S. Seki, N. Ogawa, S. Kasai, and Y. Otani, Creation of magnetic skyrmions by surface acoustic waves, Nat. Nanotechnol. **15**, 361 (2020).